

A Numerical Study of Turbulence Statistics and the Structure of a Spatially-Developing Boundary Layer Over a Realistic Urban Geometry

Atsushi Inagaki¹ · Manabu Kanda¹ · Nurul Huda Ahmad² · Ayako Yagi³ · Naoyuki Onodera⁴ · Takayuki Aoki⁵

Received: 20 March 2016 / Accepted: 11 April 2017 / Published online: 27 April 2017
© Springer Science+Business Media Dordrecht 2017

Abstract The applicability of outer-layer scaling is examined by numerical simulation of a developing neutral boundary layer over a realistic building geometry of Tokyo. Large-eddy simulations are carried out over a large computational domain (19.2 km × 4.8 km × 1 km in the streamwise, spanwise, and vertical directions, respectively), with a fine grid spacing (2 m) using the lattice-Boltzmann method with massively parallel graphics processing units. The simulation produces a ratio of the boundary-layer height to the average building height of more than 50. Results from simulations show that outer-layer features are maintained for turbulence statistics in the upper part of the boundary layer, as well as the width of predominant streaky structures throughout the entire boundary layer, despite the very large roughness. This is caused by the existence of very large streaky structures extending throughout the entire boundary layer, which follow outer-layer scaling with a self-preserving development. We assume the top-down mechanism in the physical interpretation of results.

Keywords Lattice-Boltzmann method · Outer-layer scaling · Top-down mechanism · Urban boundary layer · Very large streaky structures

✉ Atsushi Inagaki
inagaki.a.ab@m.titech.ac.jp

¹ Department of Transdisciplinary Science and Engineering, Tokyo Institute of Technology, Tokyo, Japan

² Engineering Department (Mechanical Engineering), UTM Razak School of Engineering and Advanced Technology, Universiti Teknologi Malaysia, Kuala Lumpur, Malaysia

³ Weathernews Inc., Tokyo, Japan

⁴ Center for Computational Science and e-Systems, Japan Atomic Energy Agency, Chiba, Japan

⁵ Global Scientific Informational and Computing Center, Tokyo Institute of Technology, Tokyo, Japan

1 Introduction

As urban geometry is the largest roughness feature on the Earth's surface, it is useful to examine the mechanical effects of fully-rough surface geometries on boundary-layer turbulence (e.g., Roth 2000). Although purely neutral stratification rarely occurs in the atmospheric boundary layer, it is still useful to investigate the aerodynamic role of roughness in a boundary layer for engineering applications (e.g., Macdonald et al. 1998; Barlow et al. 2004; Hagishima et al. 2009; Kanda et al. 2013).

We examine the applicability of outer-layer scaling to turbulence statistics and the properties of coherent turbulence structures within a spatially-developing boundary layer over a building array, which is a type of very rough surface (e.g., Mulhearn and Finnigan 1978). The outer layer is the upper part of the boundary layer in which the boundary-layer thickness δ is a relevant length scale. The inner layer is the lower layer extending from the ground to the top of the logarithmic layer. Turbulent flows in the inner layer over fully-rough walls are predominantly characterized by the aerodynamic roughness length z_0 (e.g., Raupach et al. 1991) rather than the viscous length scale for smooth walls. An overview of inner- and outer-layer characteristics is provided in, e.g., Raupach et al. (1991), Jiménez (2004) and Marusic et al. (2010).

Two opposing concepts have been proposed relating to the dominant mechanism governing the dynamics of the boundary layer (e.g., Raupach et al. 1991). One considers the predominance of the dynamics of the inner region, in which surface properties characterize the entire layer. The other considers the predominance of the dynamics in the outer layer, in which the outer layer controls the inner region.

The top-down mechanism (Hunt and Morrison 2000; Hunt and Carloti 2001) considers the predominance of the dynamics in the outer layer to explain the maintenance of high-Reynolds-number boundary-layer flows. To reproduce eddies with an inner-layer scaling on the basis of rapid distortion theory, impingement of detached eddies from the outer layer must be modified by the local mean wind shear and the blocking effect of solid walls (Hunt and Morrison 2000). This scenario is possible for various types of roughness because detached eddies with outer-layer scaling produce turbulent structures throughout the entire boundary layer, as supported by experimental evidence, including from field experiments (e.g., Högström et al. 2002), a wind-tunnel experiment over a flat wall with artificially detached eddies (Hattori et al. 2010), and an outdoor experiment that used a reduced urban-scale model (Inagaki and Kanda 2010). While similar examination of the top-down mechanism in real cities is rare (e.g., Fesquet et al. 2009; Horiguchi et al. 2012 for suburban areas), an examination of flow over such large roughness elements may provide strong evidence for the credibility of the top-down mechanism.

The relevance of outer-layer scaling for the entire boundary layer is also found in the scaling of the coherent structure of turbulence. A variety of previous indoor and outdoor experiments has revealed that streaky structures of streamwise velocity fluctuations appear both in the inner and outer layers over flat surfaces (e.g., Tomkins and Adrian 2003; Drobinski et al. 2004; Hutchins and Marusic 2007) and over building-type roughness (Newsom et al. 2008; Fujiyoshi et al. 2009; Inagaki and Kanda 2010; Takimoto et al. 2013; Yagi et al. 2016). Hutchins and Marusic (2007) revealed the validity of outer-layer scaling of the size of streaky structures in both the inner and outer regions of the boundary layer over flat surfaces, while also demonstrating the extension of large eddies throughout the boundary layer, referred to as 'superstructures'. While similar features are also seen over a fully roughened wall, they can be distinguished from those over flat walls because the latter is not related to the near-wall

cycle (e.g., Wallfe 1997; Jiménez and Pinelli 1999; Toh and Itano 2005). Marusic et al. (2010) mathematically reproduced turbulence statistics in the near-wall region for a wide range of Reynolds numbers using the fluctuating large-scale signals from the logarithmic region with a model function.

Over very rough surfaces, turbulence statistics within the inner layer are strongly influenced by surface roughness. However, in their numerical simulations for various values of z_0 on a flat surface, Lin et al. (1997) revealed the predominance of outer-layer scaling for the spanwise spacing of streaky structures, rather than inner-layer scaling. While Takimoto et al. (2013) and Yagi et al. (2016) showed that the width or spacing of streaky structures over building-type roughness still depends on outer-layer scaling, they also revealed that the magnitude of the mean horizontal wind shear is also a relevant parameter.

We examine the validity of outer-layer scaling in terms of the vertical distribution of turbulent statistics and the size of streaky structures in the entire urban boundary layer under neutral stratification. Moreover, we use the width of streaky structures as a measure for examining the geometrical similarity of coherent motions. Urban roughness of a very large scale is expected to significantly influence inner-layer turbulence statistics, which is useful for evaluating the robustness of outer-layer scaling.

It is also useful to analyze a spatially-developing but temporally quasi-steady boundary layer in terms of outer-layer scaling for different δ . The assumption of the self-preserving development of a turbulent boundary layer (Townsend 1965) provides the fundamental framework for persisting with outer-layer scaling, where vertical profiles of turbulence statistics in the entire layer become self-similar if normalized by δ and the freestream velocity, which is a function of x . Smalley et al. (2001) theoretically derived the requirements for accomplishing the self-preserving development of the boundary layer when the friction velocity u_* and the rate of development of the boundary layer are constant along the streamwise direction. Although these conditions are difficult to strictly satisfy in real cities, where the building geometry is heterogeneous and u_* may change horizontally, it is still useful to evaluate the robustness of self-similar profiles for the realistic urban geometry.

Numerical simulation of a spatially-developing urban boundary layer requires a huge computational domain in the streamwise direction. Jiménez (2004) indicated that δ should be about 40–50 times larger than the height of the roughness to sufficiently decouple the inner-layer and outer-layer lengths, and to form the logarithmic layer. To accomplish this computation, the lattice-Boltzmann method is used, which is efficient on a massively-parallel graphics processing unit due to the simplicity of the numerical algorithm.

2 Method

2.1 Numerical Model

2.1.1 Lattice-Boltzmann Method

We use a numerical model based on the lattice-Boltzmann method to simulate a neutral urban airflow, where a detailed description of the model is given in Onodera et al. (2013) and Wang et al. (2014). Model validation by Huda et al. (2017) demonstrates accuracy in simulating the flow around a single cube when comparing results with those from a wind-tunnel experiment and another large-eddy simulation with the same spatial resolution (Letzel et al. 2008). The prognostic equations of the model are briefly introduced below.

To simulate fluid motion, the lattice-Boltzmann method solves the discrete Boltzmann equation instead of the Navier–Stokes equation by assuming a flow composed of streaming particles as expressed by a velocity-distribution function, the spatial and temporal evolution of which is described by a prognostic equation. As particles have a finite number of velocities, particle displacement each timestep is limited to discretized computational grids. Moving particles collide and modify the translating velocity assuming an elastic collision, which accounts for the pressure gradient and diffusion at a macroscopic scale.

The prognostic equation for the velocity distribution function is

$$f_i(x + c_i \Delta t, t + \Delta t) = f_i(x, t) - \frac{1}{\tau} \{f_i(x, t) - f_i^{eq}(x, t)\} + F_i(x, t), \tag{1}$$

where f_i is the velocity-distribution function in the i direction, x is the position, t is time, Δt is the time increment, c_i is the discretized particle velocity, $f_i^{eq}(x, t)$ is the velocity-distribution function at a local equilibrium at x and t , and τ is the relaxation time. The discretization of particle velocities follows the D3Q19 model, where “D3” denotes a three-dimensional domain and “Q19” denotes 19 discrete velocities (e.g., Qian et al. 1995) according to

$$c_i = \begin{cases} (0, 0, 0) & i = 0, \\ (\pm c, 0, 0), (0, \pm c, 0), (0, 0, \pm c) & i = 1 \sim 6, \\ (\pm c, \pm c, 0), (\pm c, 0, \pm c), (0, \pm c, \pm c) & i = 7 \sim 18. \end{cases} \tag{2}$$

The collision process is modelled based on the Bhatnagar–Gross–Krook collision model (Zou and He 1996) through the term

$$f_i^{eq} = w_i \rho \left(1 + \frac{3c_i u}{c^2} x + \frac{9(c_i u)^2}{2c^4} - \frac{3u^2}{2c^2} \right), \tag{3}$$

on the right-hand side of Eq. 1, where ρ is the fluid density, u is the macroscopic velocity in a grid box, and c is the speed of sound. Depending on the displacement of particles in D3Q19, the weight factor

$$w_i = \begin{cases} 1/3 & i = 0, \\ 1/18 & i = 1 \sim 6, \\ 1/36 & i = 7 \sim 18, \end{cases} \tag{4}$$

is introduced. The relaxation time τ to achieve the local equilibrium within the collision process is described as

$$\tau = \frac{1}{2} + \frac{3\nu}{c^2 \Delta t}. \tag{5}$$

2.1.2 Implementation of the Coherent-Structure Smagorinsky Model in the lattice-Boltzmann method

Large-eddy simulation explicitly solves fluid motion larger than the grid scale, but models the subgrid-scale motion. This was also implemented into the lattice-Boltzmann model to simulate very high-Reynolds-number turbulent flow, such as urban airflow. We use a coherent-structure Smagorinsky model because of its locally defined variables and similar performance to the dynamic Smagorinsky model for turbulent channel flow (Kobayashi 2006).

The effects of subgrid-scale eddies are introduced as a form of eddy viscosity as

$$\nu_* = C \Delta^2 \left| \tilde{S} \right|, \tag{6}$$

where,

$$\tilde{S}_{ij} = \frac{1}{2} \left(\frac{\partial \tilde{u}_j}{\partial x_i} + \frac{\partial \tilde{u}_i}{\partial x_j} \right) \tag{7a}$$

and

$$|\tilde{S}| = \sqrt{2\tilde{S}_{ij}\tilde{S}_{ij}}, \tag{7b}$$

and where Δ^2 is the square of the mean length scale of the grid cell, and $\tilde{}$ denotes a grid-scale variable.

The model coefficient of the subgrid-scale eddy viscosity for the coherent-structure Smagorinsky model is

$$C = C' |F_{CS}|^{3/2}, \tag{8}$$

where

$$F_{CS} = \frac{Q}{E} \quad (-1 \leq F_{CS} \leq 1), \tag{9}$$

$$Q = -\frac{1}{2} \frac{\partial \tilde{u}_j}{\partial x_i} \frac{\partial \tilde{u}_i}{\partial x_j} \tag{10a}$$

and

$$E = \frac{1}{2} \left(\frac{\partial \tilde{u}_j}{\partial x_i} \right)^2. \tag{10b}$$

Here, C' is the model constant, which is set to 1/20. The variables Q and E are the second invariant and the magnitude of the velocity-gradient tensor, respectively. The eddy viscosity is implemented into the relaxation time as

$$\tau_* = \frac{1}{2} + \frac{3\nu_*}{c^2 \Delta t}, \tag{11a}$$

$$\nu_* = \nu_0 + \nu_t, \tag{11b}$$

where ν_0 and ν_t are the kinematic and eddy viscosities, respectively.

2.2 Methods to Estimate u_* and Other Aerodynamic Parameters

The parameters u_* and z_0 are estimated for scaling the inner-layer flow statistics for comparison with the outer-layer scaling, using three different strategies. One strategy solves the momentum-integral equation (Schlichting 1968) as shown in Eq. 12, which is derived by vertically integrating the momentum-balance equation over the entire boundary layer assuming quasi-steady flow

$$u_* = \sqrt{\frac{d}{dx} \left(U_f^2 \theta \right) + \delta_* U_f \frac{dU_f}{dx}}, \tag{12}$$

where U_f is the freestream velocity, and δ^* and θ are the displacement and the momentum thicknesses, respectively, defined as

$$\delta^* = \int_0^\infty \left(1 - \frac{U}{U_f}\right) dz \quad (13)$$

and

$$\theta = \int_0^\infty \frac{U}{U_f} \left(1 - \frac{U}{U_f}\right) dz. \quad (14)$$

Here, U is the horizontal mean wind speed at the height z , and u_* in Eq. 12 represents the total momentum deficit in a cuboid column. The displacement and momentum thicknesses represent the deficits of the volumetric flow rate and momentum flux, respectively, from the external potential flow due to the surface drag (Schlichting 1968). Equation 12 is valid regardless of the surface conditions. Both δ^* and θ are used to evaluate δ , as discussed below.

Another strategy to estimate u_* uses the total shear stress at the bottom surface, which is estimated from the linear extrapolation of the Reynolds stress from the inner layer to the ground assuming a momentum balance of the Reynolds stress and the horizontal pressure gradient above the building canopy (e.g., Castro 2007; Leonardi and Castro 2010; Kanda et al. 2013),

$$u_* = \sqrt{-\overline{u'w'}_0}, \quad (15)$$

where $\overline{u'w'}_0$ is the estimated total shear stress acting on the bottom surface. This approach is useful for built-up areas because the total shear stress is balanced not only by the Reynolds stress, but also by the momentum sink on the vertical walls of buildings within the canopy. Studies have shown the robustness of the logarithmic layer above the building-like roughness for a linearly decreasing magnitude of the vertical shear stress, from which u_* may be defined (e.g., Moriwaki and Kanda 2006; Castro 2007; Leonardi and Castro 2010; Kanda et al. 2013).

The final strategy to estimate u_* uses the square root of the maximum peak of $-\overline{u'w'}$ (e.g., Kastner-Klein and Rotach 2004), which assumes a constant-stress region around the $-\overline{u'w'}$ maximum (Rotach 2001), with the significant advantage of a simple definition and calculation.

The aerodynamic surface roughness z_0 and the displacement height d are estimated by fitting a logarithmic profile for neutral stratification to the mean horizontal wind speed,

$$\frac{U}{u_*} = \frac{1}{\kappa} \ln \frac{z-d}{z_0}, \quad (16)$$

where u_* is estimated using either of the three strategies described above.

2.3 Method for Detecting the Location of Energetically Predominant Structures Using a Wavelet Transform

We use a wavelet transform to identify the locations of the energetically predominant structures in the streamwise velocity distribution on a horizontal plane by, (i) calculating the wavelet spectra for the spanwise distribution of u' , (ii) identifying a scale with a spectral peak defined as the characteristic width of the streaks, and (iii) detecting the locations of the individual structures according to the characteristic width defined in (ii) using the wavelet transform for a Mexican hat as the wavelet function.

3 Numerical Settings

3.1 Numerical Domain and Computational Settings

The simulation dataset described in [Huda et al. \(2017\)](#) is also analyzed here, where the lower surface reflects a real urban morphology in a coastal area, with the aim of reproducing a spatially-developing neutral boundary layer in an urban area. The simulation required a large computational domain along the streamwise direction to develop the boundary layer to a sufficient height for examining the details of the layered structures within. A fine grid scale of the order of 1 m explicitly resolves individual buildings. The size of the computational domain is 19.2, 4.8, and 1 km in the streamwise, spanwise, and vertical directions, respectively, with a homogeneous and isotropic grid spacing of 2 m, as used in previous studies ([Castillo et al. 2011](#); [Inagaki et al. 2012](#); [Kanda et al. 2013](#)).

The lateral boundary conditions are periodic, where the top boundary has free-slip conditions, while the ground and walls of buildings are non-slip bounce-back boundary conditions ([Yin and Zhang 2012](#)). On the top, lateral and outlet boundaries, damping layers of 60-m thickness, where the viscosity increases linearly to 50 times the default value ($= 1.512 \times 10^{-5} \text{ m}^2 \text{ s}^{-1}$), suppress the amplification of artificial waves. Homogeneous laminar flow of speed 10 m s^{-1} representing the relatively smooth surface of the sea is implemented at the inlet surface of the boundary. An inflow turbulence generator (e.g., [Lund et al. 1998](#); [Xie and Castro 2008](#)) may effectively reduce the required size of the computational domain in the streamwise direction compared with a homogeneous inflow. However, boundary-layer development and the positions of coherent turbulence structures are triggered by artificial turbulence, and possibly persist for long distances. Hence, a homogeneous inflow is a simple means of avoiding such uncertainties, while maintaining a rigorous test for outer-layer scaling for various δ . The present inflow condition simplifies a realistic marine boundary layer in terms of roughness and buoyancy effects, with the upwind roughness negligible in this case, because the internal boundary-layer growth is mostly characterized by the rougher surface ([Jackson 1976](#)). The most critical issue is the temperature contrast between upwind and downwind locations, which may either accelerate or decelerate boundary-layer growth depending on the thermal stratification (e.g., [Garratt 1990](#)). Additionally, inflow from the marine boundary layer brings moister air, and induces cumulous clouds (e.g., [Garratt 1992](#)) above the convective mixed layer over urban areas. The buoyancy effect, including the effect of cloud formation, is beyond the scope of this study.

The simulation was conducted using the TSUBAME2.5 super computer at the Global Scientific Information and Computing Center of the Tokyo Institute of Technology with 900 graphics processing units. The timestep was 0.008 s for a total integration time of 6420 s (802,500 steps), during which the temporal development of δ reached a quasi-steady state. The final 1800 s is used for the following analysis. As a consequence of the limited computational resources, the averaging time may not have been sufficient when compared with conventional experiments (e.g., [Coceal et al. 2006](#)). All statistics are thus spatially averaged over a wide horizontal domain extending 4.8 km in the y -direction.

3.2 Morphological Characteristics of Roughness

The simulation targets a coastal area of Tokyo and Kanagawa, with [Fig. 1](#) showing the distribution of building heights in the simulation domain, reproduced using a digital building-elevation map (MAPCUBE®, CAD Center Corporation, Tokyo, Japan). The flow in the numerical domain is from left to right, and a flat surface extending 1 km from the inlet of

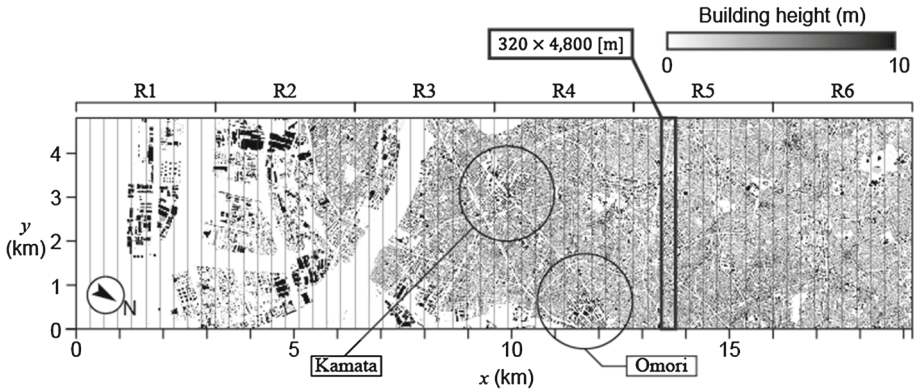


Fig. 1 Building-height distribution within the computational domain. The entire domain is separated into 60 sub-sections along the streamwise direction, and also six sections (sections R1–R6) from the inlet to outlet. Two commercial areas, Kamata and Omori, are circled

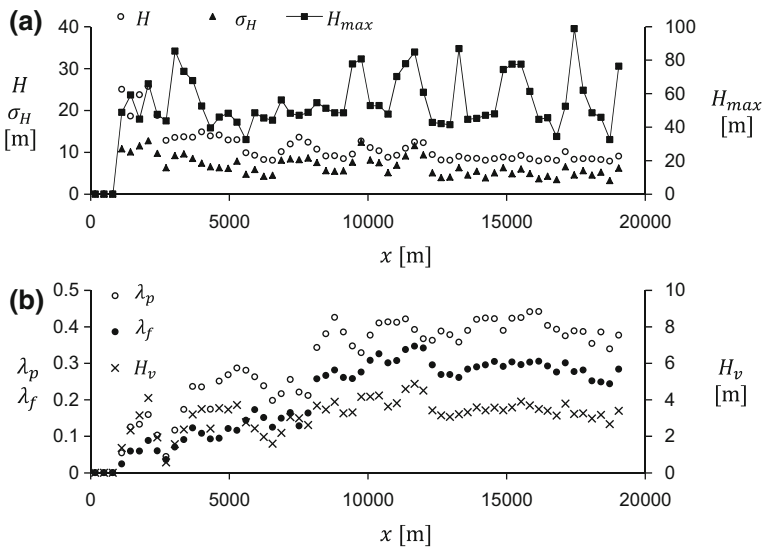


Fig. 2 Spatial distributions of **a** the average, standard deviation, and maximum building heights (H , σ_H , and H_{max} , respectively), and **b** the plan-area index λ_p , frontal-area index λ_f , and bulk ratio H_v of the buildings, within 60 sub-sections plotted along x

the computational domain prevents a return flow at the inlet surface. The maximum building height in this domain is 98 m, with an average of 11.2 m. To average flow statistics and roughness properties along the streamwise direction, 60 sub-sections with an area of $320 \times 4800 \text{ m}^2$ (see the bold boundary in Fig. 1) are defined. A further six sub-sections of $3200 \times 4800 \text{ m}^2$, and labelled R1 ~ R6 from the inlet to the outlet of the domain, are also shown in Fig. 1.

Figure 2 shows the mean statistics of the building morphology in the 60 sub-sections distributed along x : the average, standard deviation, and maximum building height (H , σ_H , and H_{max} , respectively); the plan-area index λ_p (the horizontal normal to the main stream of buildings over the gross area); the frontal-area index λ_f (the vertical area normal to the

main stream of buildings over the gross area); and the bulk ratio H_v (the total volume of buildings over the gross area). These parameters are related to the aerodynamic properties of the roughness. Many areas of reclaimed land are separated by water near the coastal area, which extends 8 km from the inlet, resulting in smaller values of λ_p and λ_f than the corresponding values further from the coast. The mean building heights H are larger in the areas of reclaimed land, because of the many large warehouses and factories, rather than the residential houses, which form the majority of buildings further inland. There are two commercial areas at Kamata ($x = 10$ km, $y = 3$ km) and Omori ($x = 11.5$ km, $y = 0.5$ km) having a large σ_H and H_v , and include several high-rise buildings.

The simulations achieved a very high Reynolds number, defined as $Re^* = Hu_*/\nu = 7.89 \times 10^5$, which is comparable with the real atmosphere (Raupach et al. 1991). Huda et al. (2017) confirmed that the present numerical model has the same accuracy as the other large-eddy simulations (Letzel et al. 2008) when simulating high-Reynolds-number turbulent flow.

4 Results

4.1 Mean Flow Characteristics

4.1.1 Boundary-Layer Development over an Urban Surface Geometry

Figure 3 shows the boundary-layer evolution along the streamwise direction as quantified as the height where the mean wind speed reaches 99% of the freestream velocity $U_f(\delta)$, the displacement thickness (δ^*), and momentum thickness (θ). Here, δ^* and θ are defined in Eqs. 13 and 14, and are calculated from the mean velocity profiles averaged within the 60 sub-sections, and over a time period of 30 min. In the entrance region, where the flat surface extends about 1 km from the inlet, δ reaches a height of about 60 m. The magnitude of δ exceeds 400 m at 15 km from the inlet resulting from the very long fetch and large roughness. The value of δ/H exceeds 40 on the downwind side at $x = 12,000$ m, where the sections R5 and R6 are located. The rate of development of δ is $\sim \Delta x^{0.67}$, where Δx is the distance along x from the building edge at the most upwind side (i.e., $x = 1162$ m) found by fitting a power law to the latter half of the domain. We find a smaller exponent than the value (= 0.8) representing the growth rate of the internal boundary layer widely observed

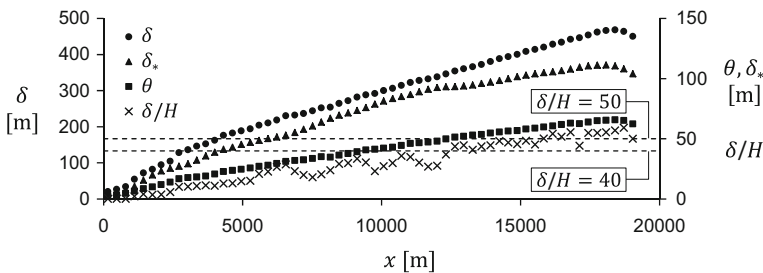


Fig. 3 Spatial development of the boundary-layer thickness defined by the level at which mean wind speed is 99% of the freestream velocity (filled circle, δ), the displacement thickness (filled triangle, δ_*), and momentum thickness (filled square, θ). The ratio of δ and the average building height is also plotted (cross, δ/H). Dashed lines show the levels at $\delta/H = 40$ and 50

in the case of a smooth-to-rough transition (Garratt 1990), or the turbulent boundary-layer growth derived by Schlichting (1968). Cheng and Castro (2002) observed a smaller growth rate than 0.8 in cases with a step change to a greater bar roughness. Although not evaluated here, Castro (2007) has shown that the spatial growth of the displacement and the momentum thicknesses follow a single curve, regardless of roughness geometry, which is accomplished by introducing the effective origin of the boundary-layer development estimated from the momentum-integral equation, assuming a universal function of the mean wind-speed profile.

The boundary-layer heights for the three different definitions monotonically increase with distance x , with the proportions being roughly $\delta^*/\delta = 0.25$ and $\theta/\delta = 0.14$ as averaged over buildings in sections R2–R6. The rate of increase in δ^* varies relative to the other two definitions, with a small ‘hump’ around $x = 8000\text{--}13,000$ m, causing large values for the shape factor (δ^*/θ) as well (not shown), which is a function of the drag coefficient (e.g., Castro 2007). The large obstacles around 8000–13,000 m result in large surface friction (see later section) and larger shape factors.

We use δ below as the outer-layer length scale because it is defined without the use of the inner-layer flow properties. The other two parameters, δ^* and θ , are still used to estimate u_* through Eq. 12.

4.1.2 Outer-Layer Scaling for the Vertical Distributions of the Mean Flow Statistics

We examine the validity of the outer-layer scaling for the vertical distribution of the mean flow statistics. The statistics for section R1 ($x = 0\text{--}3200$ m) are neglected because of the transitional surface roughness. Figure 4 shows vertical distributions of the turbulent flow

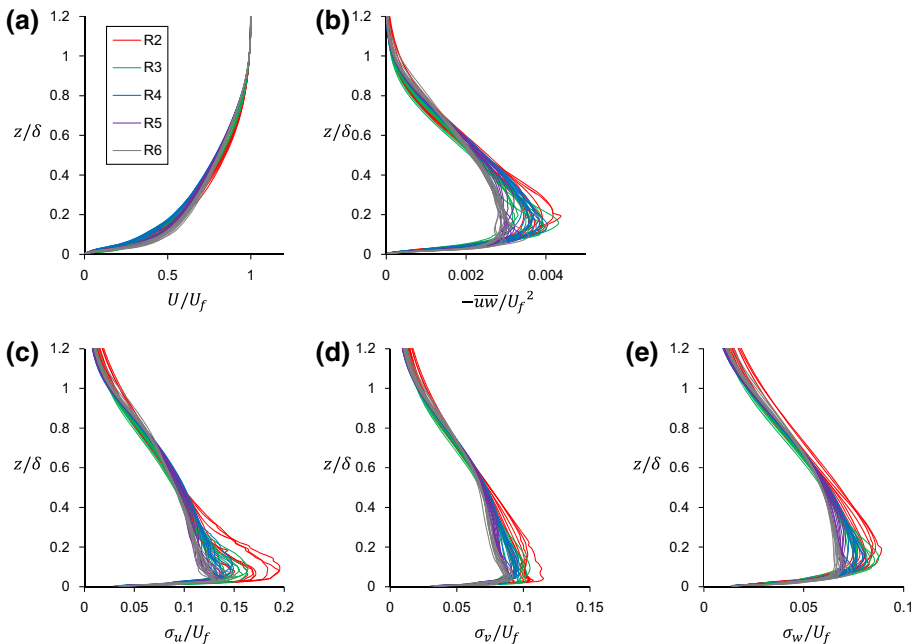


Fig. 4 Vertical distribution of mean turbulent statistics **a** U/U_f , **b** $-\overline{u'w'}/U_f^2$, **c** σ_u/U_f , **d** σ_v/U_f , **e** σ_w/U_f , averaged within the 60 sub-sections. Different averaging areas (sections R2–R6) are distinguished by different colours

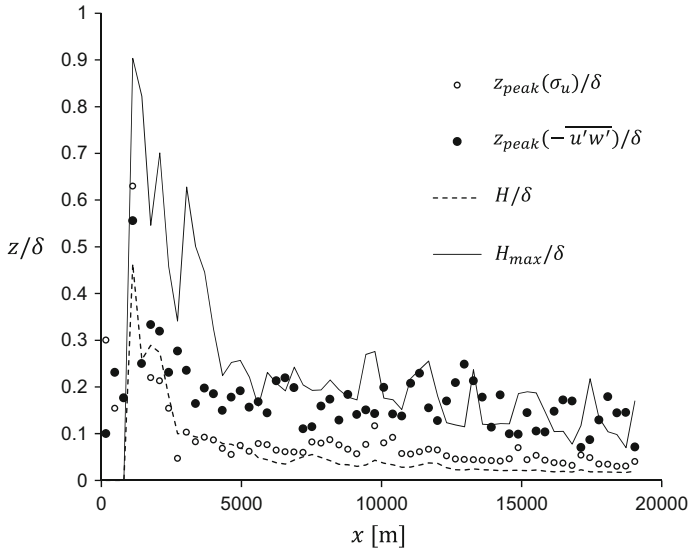


Fig. 5 Streamwise distribution of the level of the maximum peaks of σ_u (open circle) and $\overline{-u'w'}$ (filled circle) plotted together with H (dashed line) and H_{max} (solid line), normalized by δ

statistics normalized by outer-layer scaling parameters, i.e., the freestream velocity U_f and δ . The lines differentiate the positions of the profiles in the 60 sub-sections (see Fig. 1) and are coloured differently for sections R2–R6.

The vertical distributions of all non-dimensional statistics, particularly for the standard deviations of the velocity fluctuations, reduce to a single curve in the upper part of the boundary layer (above 0.6δ here). Hence, the flow in the upper layer follows outer-layer scaling and self-preserving development despite an extremely large surface roughness and horizontal heterogeneity. Outer-layer similarity is robust for $\delta/H < 40$, where the inner- and outer-layer scales are still not well decoupled as indicated by Jiménez (2004).

Profiles start to deviate from each other below about $z = 0.6\delta$, with two particular features: (i) the magnitudes of the non-dimensional standard deviations of the velocity fluctuation and the normalized momentum flux decrease with x , and (ii) the maximum peak also deviates, but does not monotonically increase or decrease with x . This layer is located within an inner layer, where turbulence statistics are affected by the surface roughness, and are not solely described by outer-layer scaling. The reason for (i) is partially attributed to the dependence on δ . We confirmed that a thinner boundary layer causes a larger vertical gradient of the mean velocity near the ground, which generates significant amounts of turbulent kinetic energy (data not shown). Here, σ_u , σ_v , and σ_w decrease with increasing δ along x , although the effect becomes smaller with increasing δ/H . The characteristics of reason (i) result in nearly constant values of the momentum flux and the standard deviations around $z = 0.2-0.4\delta$, especially at sections R5 and R6, where δ/H is <40 .

With regard to reason (ii), Fig. 5 shows the height of the maximum peak of σ_u and $\overline{-u'w'}$ at each x normalized by δ . The heights of the maximum peaks of σ_v and σ_w are almost the same as those of σ_u and $\overline{-u'w'}$, respectively (data not shown). The levels of the maximum peak of $\overline{-u'w'}$ correspond to the maximum building height, except near the inlet where H/δ is too large to neglect the direct influence of roughness on δ . Previous studies have also indicated that the maximum Reynolds stress appears near the top of the highest buildings rather than at

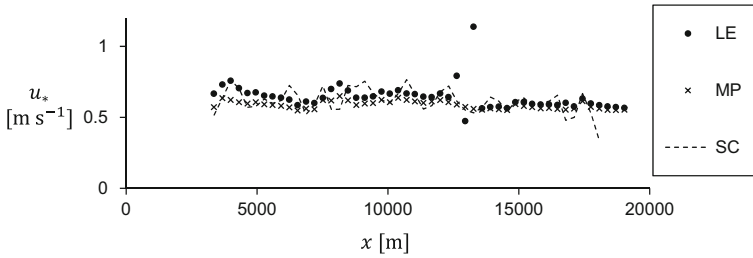


Fig. 6 Streamwise distribution of u_* estimated using three strategies: 1 the linear regression of the Reynolds stress fitted at $z = 4H - 0.4\delta$ (LE), 2 square root of the maximum peak of $-\overline{u'w'}$ (MP), and 3 from the momentum-integral equation in columns extending 320 m from the upwind side along the x direction (SC)

the average building height (e.g., Kanda 2006; Nakayama et al. 2011; Kanda et al. 2013). As taller buildings encounter higher mean wind speeds, drag is more effectively induced than for smaller buildings. For flat walls in contrast (e.g., Raupach 1981), the maximum Reynolds stress or σ_w occur much higher than the height of roughness as a result of the blocking effect of the vertical velocity fluctuation (Hunt and Morrison 2000). Therefore, the large roughness can effectively modify the shape of the Reynolds-stress profile, and will have some influence on the emergence of the Reynolds-stress constant.

The heights of the maximum peaks of σ_u are roughly 0.43 those of σ_w , and are also weakly positively correlated with the surface geometry (e.g., a linear correlation of 0.40 with the standard deviation of the building height).

4.1.3 Estimation of u_* , z_0 and d

The value of u_* is estimated (see Sect. 2.2) from (i) the integral-momentum equation (Eq. 12) (denoted as $u_{*,SC}$), (ii) the root-mean square of the maximum peak of $-\overline{u'w'}$ ($u_{*,MP}$), and (iii) the linearly extrapolated value of $-\overline{u'w'}$ to the ground ($u_{*,LE}$). The integral-momentum equation is considered for a control volume of 640 m \times 4800 m \times 600 m in the x -, y -, and z -directions, respectively. To estimate u_* from the total shear stress in Eq. 15, the vertical profile of $-\overline{u'w'}$ within a range of $z = 4H - 0.4\delta$ is linearly extrapolated to the ground (hereafter, $u_{*,LE}$), because $z = 0.4\delta$ is expected to be within the inner layer as seen in Fig. 4, and $z = 4H$ is above the roughness sublayer over a real urban geometry (e.g., Roth 2000). The same range is used to fit the logarithmic profile to the mean wind-speed distribution to estimate z_0 and d .

Figure 6 shows the spatial variation in u_* along x , where the three definitions coincide well with each other. The magnitude of $u_{*,LE}$ deviates considerably from the other values, because the taller buildings above $z = 4H$ around $x = 12,000$ m generate a large Reynolds stress near their tops. The magnitude of $u_{*,MP}$ is smaller than that calculated with the integral-momentum equation throughout most of the computational domain. This means that $u_{*,MP}$ actually underestimates the total shear stress, although the deficit is small, especially considering the large value of δ . The magnitude of $u_{*,LE}$ is closer to $u_{*,CE}$ than $u_{*,MP}$ over a major part of the domain.

Aerodynamic parameters are also estimated based on the estimated u_* shown in Fig. 6. The fitting range of the variables to Eq. 16 is between $z = 4H$ and $z = 0.4\delta$ for all cases, and is compared with the morphological parameters of the roughness for validation. Because the morphological parameters contributing to the roughness are too variable, we use the models of z_0 and d as representative of the morphological characteristics. The models of Kanda et al.

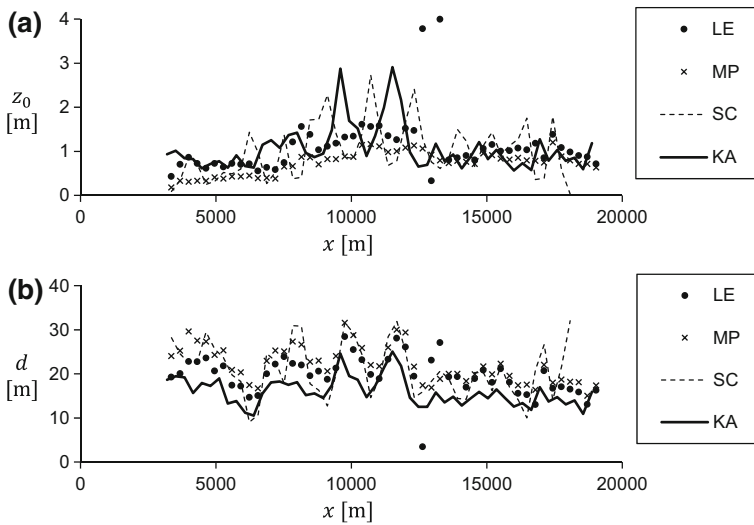


Fig. 7 Streamwise distribution of **a** roughness length, and **b** displacement height in the 60 sub-sections estimated for different u_* (LE, MP, and SC). The result of the morphological model developed by Kanda et al. (Kanda et al. (2013) (KA) is also plotted (*bold line*)

(2013) are used for this comparison because they account for the complex urban geometries in real cities, especially the height variation of the buildings.

Figure 7 shows z_0 and d for the three different definitions of u_* , where z_0 is found to be sensitive to the magnitude of u_* (Fig. 7a) consistent with the direct numerical simulations of Leonardi et al. (2003) and Leonardi and Castro (2010). All estimated z_0 values have a spatial variation similar to the modelled values, implying the accurate reflection of the aerodynamic characteristics of the roughness geometries. The maximum peaks of z_0 around $x = 9,000\text{--}12,000$ m of the model of Kanda et al. (2013) (KA) are located about $x = 800\text{--}1,000$ m upwind from the estimated values from the $\overline{u'w'}$ profile, because the source area of the $\overline{u'w'}$ profile at a specific height is located on the upwind side. Based on the model of Kljun et al. (2015), the point of the maximum flux contribution at the ground is located 800 m upwind of the profile at $z = 0.4\delta$. This is reasonable because the source area extends more towards the upwind side from the point of the maximum contribution.

While the estimated d values also display a similar trend to the model values, they are higher than the modelled values. We confirmed that the estimated d is smaller for a lower limit of the fitting range to the mean wind-speed profile (data not shown). Because u_* and z_0 are robust regardless of the fitting range, we continue the following discussion using u_* estimated from the maximum peak of $-\overline{u'w'}$. Our conclusion is, however, independent of the definition of u_* .

4.2 Scaling of the Width of Streaky Structures Within the Streamwise Velocity Distribution

4.2.1 Scaling of the Width of Streaky Structures

The vertical distributions of the characteristic widths of streaks from the two-point correlation are examined for various δ and compared with: (i) wind-tunnel experimental data over a flat

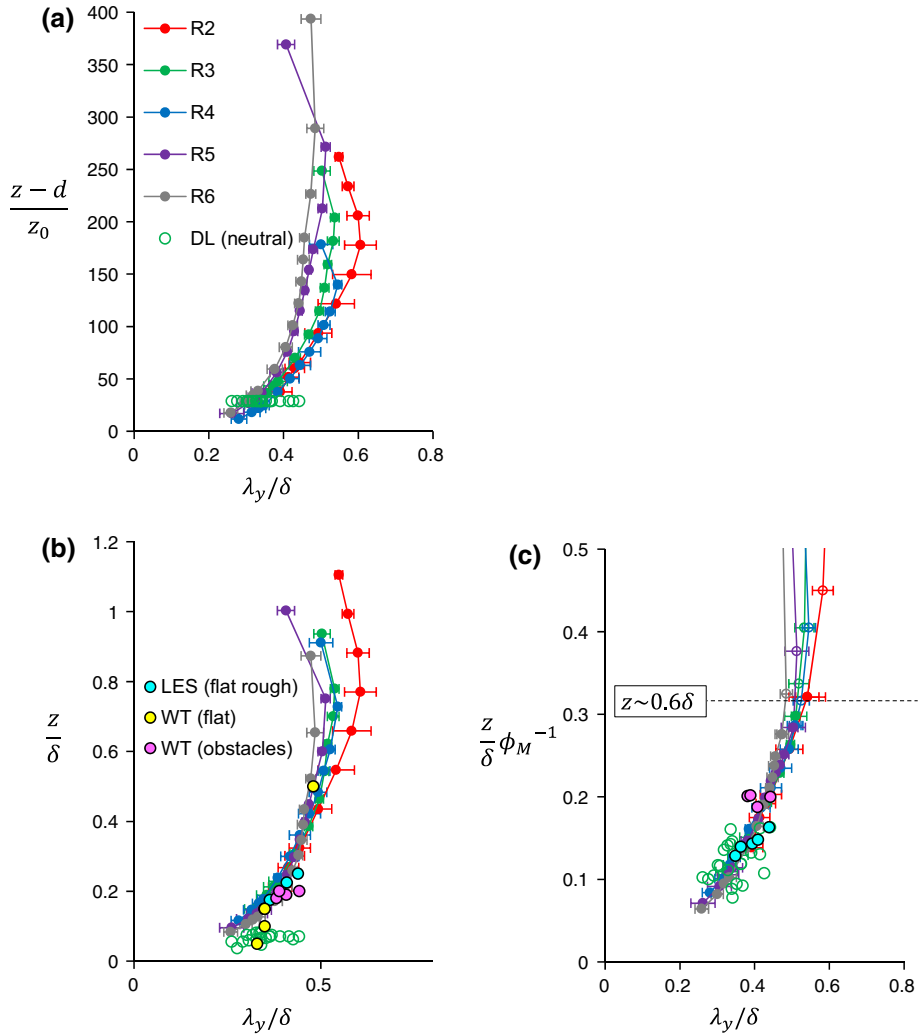


Fig. 8 Vertical distribution of λ_y/δ plotted on **a** $(z - d)/z_0$, **b** z/δ , and **c** $z/(\delta\phi_m)$ for different averaging areas (sections R2–R6). Line colours are the same as in Fig. 4, and the dots of open circles are from Doppler lidar observations (DL) under neutral stratification, as provided by Yagi et al. (2016). For **b**, **c**, filled symbols are obtained from the literature: a large-eddy simulation over flat and rough walls (light blue, Lin et al. 1997), a wind-tunnel experiment over massive obstacles (pink, Takimoto et al. 2013), and experiments over a flat surface (yellow, Hutchins and Marusic 2007)

surface (Hutchins and Marusic 2007), with results obtained over massive obstacles, including cubical and two-dimensional bars (Takimoto et al. 2013); (ii) another large-eddy simulation over flat and rough surfaces (Lin et al. 1997); (iii) results for an outdoor environment using a scanning Doppler lidar, which measured the horizontal velocity distribution at 55 m from the ground in the same urban district as this study (Yagi et al. 2016).

Figure 8 shows the vertical distribution of the non-dimensional widths of the coherent structures defined as the positive and negative separation distances between the minimum peaks of the two-point correlation of streamwise velocity component λ_y . This definition is

used because it lacks any empirical threshold, and has a simple physical meaning, which is the distance between the most energetic structures. We find that δ scales the results better than z_0 , which is consistent with previous findings (e.g., Lin et al. 1997). As we consider various surface geometries, this indicates that the widths of the coherent structures have self-preserving characteristics throughout the entire boundary layer, irrespective of very large roughness. The values near the top of the boundary layer deviate for different averaging areas, probably due to the weak velocity signal in this region and/or intermittent features of the wake interface, which leads to statistical uncertainties with respect to the spacing of the turbulent structures. This issue is discussed in more detail below.

Realistically, the Coriolis force becomes significant a few hundred metres from the ground. Lin et al. (1997) introduced the Coriolis force in their thermally neutral simulation and developed a boundary layer that extended almost 500 m above the ground. However, the similarity of the widths of the streaky structures is still robust in terms of the outer-layer scaling as shown by Yagi et al. (2016).

The widths of streaky structures observed within the atmospheric surface layer differed from the numerical results under δ scaling for both the height and width of the streaks (Fig. 8b). One reason for this is the difference in the characteristics of the outer layer. In the daytime boundary layer, buoyancy is usually the predominant force within the upper part of the layer, even for a neutral surface layer (e.g., windy conditions). While it is not immediately obvious whether the relationship between δ and λ_y within the surface layer remains consistent under different driving forces within the outer layer, it becomes comparable if a modification in the local mean wind shear is introduced to the non-dimensional height. Yagi et al. (2016) proposed $z/(\delta\phi_m)$, where $\phi_m = (\kappa z/u_*) dU/dz$ (Fig. 8c), and z/δ is the relative height of the whole boundary-layer thickness used in, e.g., Lin et al. (1997) and Hutchins and Marusic (2007). Other numerical and wind-tunnel experiments produce a similar scaling, although the plots of Hutchins and Marusic (2007) are omitted because the value of ϕ_m was not reported. The non-dimensional height $z/(\delta\phi_m)$ is composed of height-dependent local variables such as z and dU/dz , and height-independent variables such as u_* and δ . This parameter accounts for the stretching effect on the coherent structures by the local mean wind shear (e.g., Takimoto et al. 2013), which is a variable in terms of the vertical position in the boundary layer and atmospheric stability. Surface-layer data under stable and unstable stratifications also follow a single curve after this modified height scaling, as confirmed by Yagi et al. (2016). Since this non-dimensional height is the product of the inverse of dU/dz , this scaling is inappropriate near the top of the boundary layer where $dU/dz \approx 0$.

4.2.2 Detection of the Specific Streaky Structures of Energetically Predominant Eddies

While turbulence statistics in the inner layer (below about $z = 0.6\delta$) do not entirely follow outer-layer scaling, the width of streaky structures defined by the two-point correlation do follow outer-layer scaling. How streaky structures populate the inner and outer layers is examined by checking the positions of the energetically predominant structures in three layers of the rear quarter of the domain ($x = 14\text{--}19.2$ km) using the wavelet transform, as explained in Sect. 2.3.

Figure 9a shows an example of the horizontal distribution of instantaneous u at a height of 198 m. Structures appear around at 4 km downstream from the inlet, where the boundary-layer height equals the level of this horizontal cross-section; the spanwise width of streaky structures becomes thicker downstream. Figure 9b presents the contour of the pre-multiplied wavelet spectra of the variation of u' along y . The white circles in the figure represent the local maxima of the spectral energy, whose scale is considered to be the spanwise length of

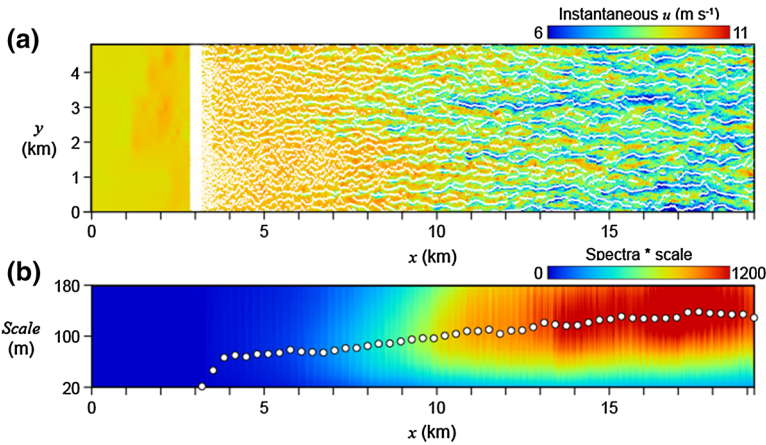


Fig. 9 An example of the horizontal distribution of instantaneous streamwise velocity component at a height of 198 m. The white lines in the upper figure show the peaks of negative u' along the spanwise direction as detected by wavelet analysis. The bottom figure shows the scaled pre-multiplied wavelet-scalogram distribution plotted as x versus scale. The white dots in the bottom panel show the peak scale (m) of u' along the spanwise direction

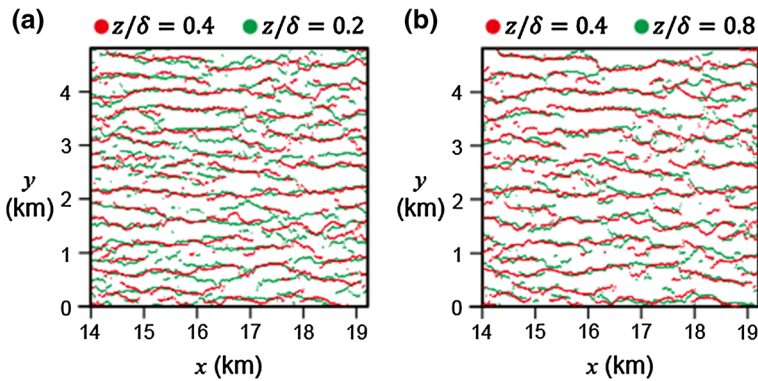


Fig. 10 Locations of the negative peaks of the streamwise velocity fluctuation corresponding to the width of the energetically predominant structures at **a** $z/\delta = 0.4$ ($z = 158$ m) and $z/\delta = 0.2$ ($z = 78$ m), **b** $z/\delta = 0.4$ and $z/\delta = 0.8$ ($z = 298$ m)

the energetically predominant structures. Also evident is a gradual increase in the width of the streaky pattern along x . The white lines in Fig. 9a represent the locally negative peaks of a smoothed velocity field using a wavelet transform with a scale according to the size of the predominant structures shown in Fig. 9b. The white lines mostly overlap with the low-momentum region of u .

This method is used to identify the locations of the predominant structures in three layers: $z = 0.2\delta$ (78 m), $z = 0.4\delta$ (158 m), and $z = 0.8\delta$ (298 m). The positions of the low-momentum regions at $z = 0.8\delta$ and $z = 0.4\delta$ coincide well with each other (Fig. 10b), indicating that identical structures of large contributions of turbulent kinetic energy extend between these layers. For the comparison of $z = 0.4\delta$ with $z = 0.2\delta$, the positions of the structures at $z = 0.4\delta$ almost overlap with those at $z = 0.2\delta$, although the energetically predominant structures at $z = 0.2\delta$ are more populated than in the upper layers. While this

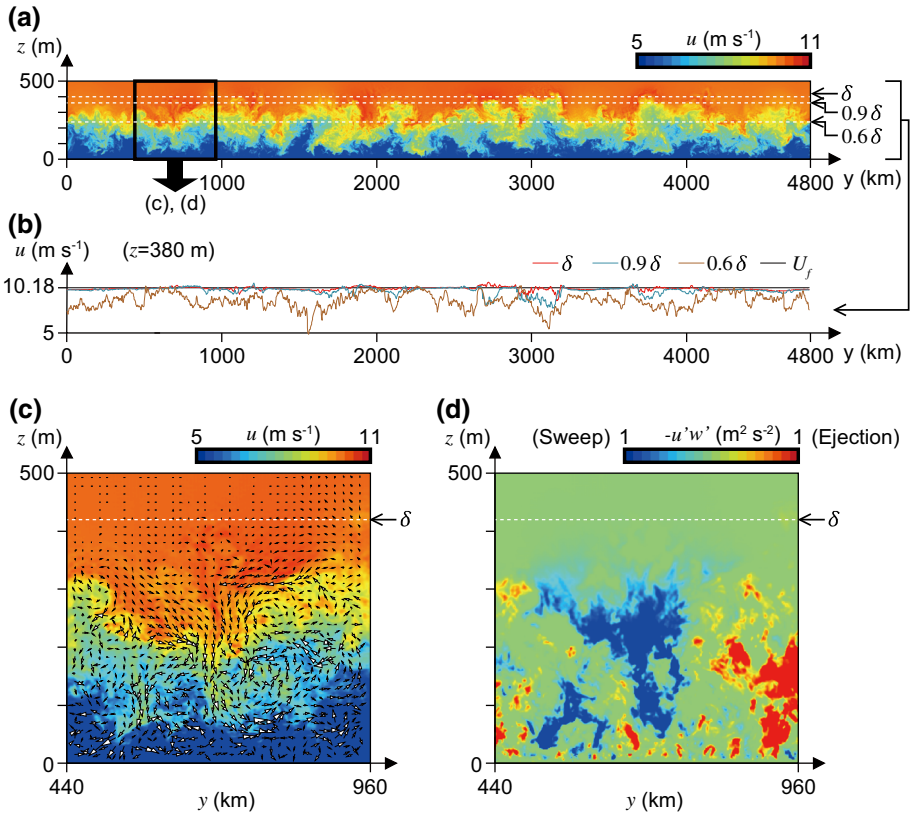


Fig. 11 Distribution of u and $-u'w'$: **a** u on the yz plane, **b** u along the y direction at $z = \delta$, $z = 0.9\delta$ and $z = 0.6\delta$, **c**, **d** magnified view of the contour of u and $-u'w'$ on the yz plane at $y = 440$ – 960 m

implies that the large structures seen in the upper layers are vertically coherent throughout the entire boundary layer, more diverse structures are found in the lower layer.

Figure 11 shows the contour of u on the yz plane at $x = 15$ km, with three traverse-lines along y at three levels (i.e., $z = \delta$, $z = 0.9\delta$ and $z = 0.6\delta$), and a magnified view of part of the plane ($y = 440$ – 960 m) with the velocity vector and the momentum flux. The momentum-flux distribution is coloured to represent the strength of ejections (red) and sweeps (blue). Turbulent flow within the boundary layer is organized into large-scale structures, which are regions of lower momentum relative to those at the same level. These structures account for the δ -scale structures shown in Fig. 10b. Meanwhile, high-speed regions in the upper part of the layer extend continuously to the external layer. Figure 11b shows that u in the high-speed regions has almost the same magnitude as U_f , and also that the flow is less turbulent in high-speed regions than in the low-speed regions. These spatially intermittent patterns are relevant to the calculated λ_y near the top of the boundary layer shown in Fig. 8. Figure 11a also shows that several high-speed regions penetrate into the lower half of the boundary layer by maintaining the magnitude of momentum of the external layer (e.g., $y = 1400$ and $y = 3700$ m in Fig. 11a, b), which is accompanied by a sweeping motion down to the ground (Fig. 11c, d). The distribution of vectors on the yz plane (Fig. 11c) indicates that a

strong sweep occurs with a weak horizontal convergence within the outer layer between the magnified low-speed regions.

5 Implication for the Top-Down Mechanism

This section considers the physical interpretation of the numerical results in the framework of the top-down mechanism.

Very large streaky structures are potential candidates for the detached eddies in the top-down mechanism because: (i) they have the size of the outer-layer length scale δ , and (ii) they impinge on the ground as sweeping motions (Figs. 10, 11). The impingement from the outer layer seems to occur between the very large streaky structures of low-momentum regions in the outer layer, because two structures next to each other entrain air from the external layer down to the ground (Fig. 11), while resembling bulge structures (e.g., [Brown and Thomas 1977](#)). [Takimoto et al. \(2013\)](#) also demonstrated that the high-speed regions of very large streaky structures are less turbulent than the low-speed regions.

There is no clear evidence of the blocking and shearing effect on the ground that causes smaller eddies to burst up, which is referred to as 'anti-splats'. One reason for this is that eddies may be disturbed by wake motions from the building edges, which are particularly strong on the roofs of the taller buildings (Fig. 5). In a case with a regular array of homogeneous cubes, impingement from the outer layer to the ground, and also the bursting-up from the building canopy, has clearly been shown under mixed-layer convection ([Inagaki et al. 2012](#)), while the turbulent statistics still retain their universal relationship with the inner-layer parameters ([Castillo et al. 2011](#)) as predicted from wall-turbulence similarity ([Townsend 1976](#)). While this supports the validity of the shearing and blocking effect of the top-down mechanism, further justification for a variety of building geometries is required.

6 Conclusions

Our numerical study considered the applicability of outer-layer scaling of turbulence statistics, and the spanwise width of coherent structures within a spatially-developing boundary layer over urban roughness. Although the large roughness tends to lead to a strong influence of boundary-layer turbulence to inner-layer scaling, the outer-layer characteristics are maintained for both turbulence statistics beyond the inner layer, as well as the spacing of streaky structures. In the case of low δ/H , the magnitude of the turbulence intensity in the inner layer is also described by outer-layer scaling.

We have also shown that there are energetically predominant structures throughout the entire boundary layer, which probably contribute to the entire flow dynamics within the boundary layer. However, the dynamics that sustain the turbulent kinetic energy of these large structures remain unclear. This is related to the fundamental question of whether the dynamics of the inner or outer layer are predominant in high-Reynolds-number boundary layers over rough surfaces, or in other words, whether the top-down or bottom-up mechanism is predominant.

As another perspective of the effects of roughness, [Park et al. \(2015\)](#) demonstrated that high-rise buildings trigger the very large-scale motion of low-momentum regions, extending a few kilometres downstream from buildings. The question of what kind of environment is required to generate streaky structures from buildings and when they are generated is

important, because they are not always seen behind the same high-rise buildings (Yagi et al. 2016). The answers to these questions would lead to an understanding of the passive control of streaky structures, and, in turn, the atmospheric environment in the urban boundary layer, because they are closely related to dispersion in and above the urban canopy.

Acknowledgements This study was financially supported by JSPS KAKENHI Grant Numbers 25249066, 26420492, and 50614484, and partially supported by the Joint Usage/Research Center for Interdisciplinary Large-scale Information Infrastructures and High-Performance Computing Infrastructure in Japan. We also thank Dr. H. Sugawara (National Defense Academy) for advising us about the calculation of the source area, and Mr. S. Sumiyoshi (Tokyo Institute of Technology) for data processing.

References

- Barlow JF, Harman IN, Belcher SE (2004) Scalar fluxes from urban street canyons. Part I: laboratory simulation. *Boundary-Layer Meteorol* 113(3):369–385
- Brown GL, Thomas ASW (1977) Large structure in a turbulent boundary layer. *Phys Fluids* 20:S243
- Castillo MC, Inagaki A, Kanda M (2011) The effects of inner- and outer-layer turbulence in a convective boundary layer on the near-neutral inertial sublayer over an urban-like surface. *Boundary-Layer Meteorol* 140(3):453–469
- Castro IP (2007) Rough-wall boundary layers: mean flow universality. *J Fluid Mech* 585:469–485
- Cheng H, Castro IP (2002) Near wall flow over urban-like roughness. *Boundary-Layer Meteorol* 104(2):229–259
- Coccal O, Thomas TG, Castro IP, Belcher SE (2006) Mean flow and turbulence statistics over groups of urban-like cubical obstacles. *Boundary-Layer Meteorol* 121:491–519
- Drobinski P, Carlotti P, Newsom RK, Banta RM, Foster RC, Redelsperger JL (2004) The structure of the near-neutral atmospheric surface layer. *J Atmos Sci* 61(6):699–714
- Fesquet C, Dupont S, Drobinski P, Dubos T, Barthlott C (2009) Impact of terrain heterogeneity on coherent structure properties: numerical approach. *Boundary-Layer Meteorol* 133(1):71–92
- Fujiyoshi Y, Yamashita K, Fujiwara C (2009) Detection of organized airflow in the atmospheric boundary layer and the free atmosphere using a 3D-scanning coherent Doppler lidar. In: International symposium on photoelectronic detection and imaging 17–19 June 2009, Beijing China, pp 738204–738204
- Garratt JR (1990) The internal boundary layer: a review. *Boundary-Layer Meteorol* 50:171–203
- Garratt JR (1992) The atmospheric boundary layer. Cambridge University Press, Cambridge, 316 pp
- Hagishima A, Tanimoto J, Nagayama K, Meno S (2009) Aerodynamic parameters of regular arrays of rectangular blocks with various geometries. *Boundary-Layer Meteorol* 132(2):315–337
- Hattori Y, Moeng C-H, Suto H, Tanaka N, Hirakuchi H (2010) Wind-tunnel experiment on logarithmic-layer turbulence under the influence of overlying detached eddies. *Boundary-Layer Meteorol* 134(2):269–283
- Högström U, Hunt JCR, Smedman A (2002) Theory and measurements for turbulence spectra and variances in the atmospheric neutral surface layer. *Boundary-Layer Meteorol* 103:101–124
- Horiguchi M, Hayashi AT, Adachi A, Onogi S (2012) Large-scale turbulence structures and their contributions to the momentum flux and turbulence in the near-neutral atmospheric boundary layer observed from a 213-m tall meteorological tower. *Boundary-Layer Meteorol* 144(2):179–198
- Huda AN, Inagaki A, Kanda M, Onodera N, Aoki T (2017) Large eddy simulation of the gust index in an urban area using the lattice Boltzmann method. *Boundary-Layer Meteorol*. doi:10.1007/s10546-017-0233-6
- Hunt JCR, Morrison JF (2000) Eddy structure in turbulent boundary layers. *Eur J Mech B Fluids* 19:673–694
- Hunt JCR, Carlotti P (2001) Statistical structure at the wall of the high Reynolds number turbulent boundary layer. *Flow Turb Combust* 66:453–475
- Hutchins N, Marusic I (2007) Evidence of very long meandering features in the logarithmic region of turbulent boundary layers. *J Fluid Mech* 579:1–28
- Inagaki A, Kanda M (2010) Organized structure of active turbulence over an array of cubes within the logarithmic layer of atmospheric flow. *Boundary-Layer Meteorol* 135:209–228
- Inagaki A, Castillo MC, Yamashita Y, Kanda M, Takimoto H (2012) Large-eddy simulation of coherent flow structures within a cubical canopy. *Boundary-Layer Meteorol* 142(2):207–222
- Jackson PS (1976) The propagation of modified flow downstream of a change in roughness. *Q J R Meteorol Soc* 102:924–933
- Jiménez J (2004) Turbulent flows over rough walls. *Annu Rev Fluid Mech* 36:173–196
- Jiménez J, Pinelli (1999) The autonomous cycle of near-wall turbulence. *J Fluid Mech* 389:335–359

- Kanda M (2006) Large-eddy simulations on the effects of surface geometry of building arrays on turbulent organized structures. *Boundary-Layer Meteorol* 118(1):151–168
- Kanda M, Inagaki A, Miyamoto T, Gryschka M, Raasch S (2013) A new aerodynamic parametrization for real urban surfaces. *Boundary-Layer Meteorol* 148(2):357–377
- Kastner-Klein P, Rotach MW (2004) Mean flow and turbulence characteristics in an urban roughness sublayer. *Boundary-Layer Meteorol* 111(1):55–84
- Kljun N, Calanca P, Rotach MW, Schmid HP (2015) A simple two-dimensional parameterisation for Flux Footprint Prediction (FFP). *Geosci Model Dev* 8:3695–3713
- Kobayashi H (2006) Large eddy simulation of magnetohydrodynamic turbulent channel flows with local subgrid-scale model based on coherent structures. *Phys Fluids* 18:045107
- Leonardi S, Orlandi P, Smalley RJ, Djenidi L, Antonia RA (2003) Direct numerical simulations of turbulent channel flow with transverse square bars on one wall. *J Fluid Mech* 491:229–238
- Leonardi S, Castro IP (2010) Channel flow over large cube roughness: a direct numerical simulation study. *J Fluid Mech* 651:519–539
- Letzel MO, Krane M, Raasch S (2008) High resolution urban large-eddy simulation studies from street canyon to neighbourhood scale. *Atmos Environ* 42(38):8770–8784
- Lin CL, Moeng CH, Sullivan PP, McWilliams JC (1997) The effect of surface roughness on flow structures in a neutrally stratified planetary boundary layer flow. *Phys Fluids* 9:3235–3249
- Lund TS, Wu X, Squires KD (1998) Generation of turbulent inflow data for spatially developing boundary layer simulations. *J Comp Phys* 140:233–258
- Marusic I, Mathis R, Hutchins N (2010) Predictive model for wall-bounded turbulent flow. *Science* 329:193–196
- Macdonald RW, Griffiths RF, Hall DJ (1998) An improved method for the estimation of surface roughness of obstacle arrays. *Atmos Environ* 32:1857–1864
- Moriwaki R, Kanda M (2006) Flux-gradient profiles for momentum and heat over an urban surface. *Theor Appl Climatol* 84:127–135
- Mulhearn PJ, Finnigan JJ (1978) Turbulent flow over a very rough random surface. *Boundary-Layer Meteorol* 15(1):109–132
- Nakayama H, Takemi T, Nagai H (2011) LES analysis of the aerodynamic surface properties for turbulent flows over building arrays with various geometries. *J Appl Meteorol Climatol* 50(8):1692–1712
- Newsom R, Calhoun R, Ligon D, Allwine J (2008) Linearly organized turbulence structures observed over a suburban area by dual-Doppler lidar. *Boundary-Layer Meteorol* 127(1):111–130
- Onodera N, Aoki T, Shimokawabe T, Kobayashi H (2013) Large-scale LES wind simulation using lattice Boltzmann method for a 10 km × 10 km area in metropolitan Tokyo. *Tsubame ESJ* 9:2–8
- Park SB, Baik JJ, Han BS (2015) Large-eddy simulation of turbulent flow in a densely built-up urban area. *Environ Fluid Mech* 15:235–250
- Qian YH, Succi S, Orszag SA (1995) Recent advances in lattice Boltzmann computing. *Annu Rev Comp Phys* 3:195–242
- Raupach MR (1981) Conditional statistics of Reynolds stress in rough-wall and smooth-wall turbulent boundary layers. *J Fluid Mech* 108:363–382
- Raupach MR, Antonia RA, Rajagopalan S (1991) Rough-wall turbulent boundary layers. *Appl Mech Rev* 44:1–25
- Rotach MW (2001) Simulation of urban-scale dispersion using a Lagrangian stochastic dispersion model. *Boundary-Layer Meteorol* 99(3):379–410
- Roth M (2000) Review of atmospheric turbulence over cities. *Q J R Meteorol Soc* 126:941–990
- Schlichting H (1968) *Boundary-layer theory*, 6th edn. McGraw-Hill, New York, 747 pp
- Smalley RJ, Antonia RA, Djenidi L (2001) Self-preservation of rough-wall turbulent boundary layers. *Eur J Mech B Fluids* 20:591–602
- Takimoto H, Inagaki A, Kanda M, Sato A, Michioka T (2013) Length-scale similarity of turbulent organized structures over surfaces with different roughness types. *Boundary-Layer Meteorol* 147(2):217–236
- Toh S, Itano T (2005) Interaction between a large-scale structure and near-wall structures in channel flow. *J Fluid Mech* 524:249–262
- Tomkins CD, Adrian RJ (2003) Spanwise structure and scale growth in turbulent boundary layers. *J Fluid Mech* 490:37–74
- Townsend AA (1965) Self-preserving development within turbulent boundary layers in strong adverse pressure gradients. *J Fluid Mech* 23:767–787
- Townsend AA (1976) *The structure of turbulent shear flow*. Cambridge University Press, Cambridge, 429 pp
- Wallfö F (1997) On a self-sustaining process in shear flows. *Phys Fluids* 9:883–900

- Wang X, Shangguan Y, Onodera N, Kobayashi H, Aoki T (2014) Direct numerical simulation and large eddy simulation on a turbulent wall-bounded flow using lattice Boltzmann method and multiple GPUs. *Math Problems Eng* 2014: 742432 p 10
- Yagi A, Inagaki A, Kanda M, Fujiwara C, Fujiyoshi Y (2016) Nature of streaky structures in urban boundary layer. *Bound Layer Meteorol* 163(1):19–40
- Yin X, Zhang J (2012) An improved bounce-back scheme for complex boundary conditions in lattice Boltzmann method. *J Comput Phys* 231:4295–4303
- Xie Z-T, Castro IP (2008) Efficient generation of inflow conditions for large eddy simulation of street-scale flows. *Flow Turbul Combust* 81:449–470
- Zou Q, He X (1996) On pressure and velocity flow boundary conditions and bounceback for the lattice Boltzmann BGK model. [arXiv:comp-gas/9611001](https://arxiv.org/abs/comp-gas/9611001)